Achieving high-precision ground-based photometry for transiting exoplanets

Olivier Guyon[a,b] and Frantz Martinache[a]

[a]Subaru Telescope, National Astronomical Observatory of Japan, 650 N. A'ohoku Plane, Hilo, HI 96720, USA;
[b]Steward Observatory, University of Arizona, 933 N. Cherry Ave, Tucson, AZ 85721, USA

ABSTRACT

Detection of transiting exoplanets requires high precision photometry, at the percent level for giant planets and at the 1e-5 level for detection of Earth-like rocky planets. Space provides an ideally stable - but costly - environment for high precision photometry. Achieving high precision photometry on a large number of sources from the ground is scientifically valuable, but also very challenging, due to multiple sources of errors. These errors can be greatly reduced if a large number of small wide field telescopes is used with an adequate data analysis algorithm, and the recent availability of low cost high performance digital single lens reflex (DSLR) cameras thus provides an interesting opportunity for exoplanet transit detection. We have recently assembled a prototype DSLR-based robotic imaging system for astronomy, showing that robotic high imaging quality units can be build at a small cost (under \$10000 per $deg^2 m^2$ of etendue), allowing multiple units to be built and operated. We demonstrate that a newly developed data reduction algorithm can overcome detector sampling and color issues, and allow precision photometry with these systems, approaching the limit set by photon noise and scintillation noise - which can both average as the inverse square root of etendue. We conclude that for identification of a large number of exoplanets, a ground-based distributed system consisting of a large number of DSLR-based units is a scientifically valuable cost-effective approach.

Keywords: Photometry, Exoplanets

1. INTRODUCTION

Detection of exoplanets by transit photometry, and derivation of the statistical properties of planetary systems, requires high precision photometry of a large number of stars. Due to the small photometric signature of transiting exoplanets, the measurement is challenging. Table 1 lists the main challenges to achieving high precision photometry of a large number of sources. The sources of errors fall in three broad categories:

- **Photon noise** is a fundamental limit, common to both space and ground. For a transit survey, it can only be mitigated by the survey etendue (product of collecting area and field of view), regardless of how this etendue is achieved (many individual units pointing in the same direction or a single unit).
- **Atmospheric effects** can reduce both the efficiency of the survey (fraction of cloudy weather) and its accuracy (differential extinction, color effects, PSF variations coupled with intrument). A fundamental limitation is imposed by scintillation, which cannot easily be calibrated (it is largely incoherent between sources in a wide field image), and can therefore be most efficiently mitigated by survey etendue. At fixed etendue, atmospheric effects are best reduced if multiple units are used, as most atmospheric effects are decorrelated between units (scintillation, PSF shape). Variation in sky extinctions will favor geographically separated units
- **Instrumental effects** need to be compensated for by proper calibration and data reduction. They can be mitigated by deploying multiple units, provided that instrumental errors are uncorrelated between units.

Table 1. Common sources of error in ground-based photometry, and mitigation strategy

Error Term	**Mitigation**
Atmospheric Scintillation	Large etendue, multiple units
Weather, daytime	Multiple sites, good sites
Photon noise	Large Etendue, small PSF (for faint sources only)
Variable extinction	Multiple sites, calibration, multicolor imaging
Static detector defects	Stable pointing, calibration, multiple units
Dynamic detector defects	Calibration, multiple units
Tracking errors	Guiding, Calibration, multiple units
Differential tip-tilt	multiple units, large instrumental PSF
PSF variations	large instrumental PSF, multiple units
Source blending, confusion	calibration, PSF shape analysis, multicolor imaging, small PSF

Almost all of the instrumental errors are highly unlikely to be correlated between separate telescopes (also described as units in this paper), with the exception of variable extinction, weather, daytime interruptions and source blending/confusion. The strategy we choose to explore in this paper for a transit survey is therefore to:

- (1) Achieve a large etendue per unit, and deploy multiple units, if possible at multiple sites. The final photometric accuracy is achieved by averaging by averaging the measurements from several units to achieve the final required precision. **This is a cost per etendue challenge**, and we discuss it in section 2.
- (2) Reduce, for each unit, the instrumental error - if possible down to the limit imposed by non-instrumental error sources (scintillation, photon noise, variable extinction). **This is calibration challenge**, and we discuss our approach to solve it in section 3.

To validate this approach, a prototype was assembled and operated since Jan 2011 at the Mauna Loa observatory. The prototype, described in section 2, relies on inexpensive commercially available hardware. A key goal of our project is to demonstrate that low-cost digital single lens reflex camera (DSLR) using color CMOS arrays are suitable for precision photometric measurement. Photometric measurements have previously been reported using such devices,[1, 2] and their low cost per pixel is very attractive for astronomical research.[3]

2. DEMONSTRATING LOW COST, HIGH RELIABILITY AND LARGE ETENDUE WITH A COMMERCIAL DSLR CAMERA BASED SYSTEM

2.1 Main choices and prototype 1 system description

The prototype 1 system consists of a commercial digital camera (model Canon 500D, with IR-blocking filter replaced to increase sensitivity in the red channel) with a 85mm focal length lens at F1.2 (Canon EF 85mm f/1.2L II USM). The camera is mounted on a 2-axis motorized equatorial mount (Orion Atlas EQ-G). The system (camera + mount) is computer controlled with a laptop. The data is stored on the laptop hard drive and copied to an external hard drive for retrieval. The system images are 150 square degree per frame (10 x 15 deg) with 10 arcsec square pixels. A single 4mn exposure reaches $m_V \approx 15.5$ point source detection sensitivity (no Moon). The exposure time ranges from 1mn to 6mn depending on Moon phase, and are always photon-noise limited on the sky background. The data volume is approximately 2 GB per night, stored locally. The data is physically retrieved every 2 month by copying it to an external drive (2 month of data = 120 GB). The average total power consumption is about 20W (including approximately 10W for laptop) at night, and 10W during the day

---

Further author information: (Send correspondence to O.Guyon)
O.Guyon: E-mail: guyon@naoj.org

Figure 1. Two views of the prototype 1 system, which is mounted on the side of the VYSOS computer building. The total volume of the system is a 67 cm diameter, 35 cm tall cylinder (painted white). The bottom part of the volume consists of the electronics plate, the top part is a platform which holds the mount and the camera. The laptop computer is located inside the building on which the unit is mounted. In both images, the camera is pointing down, which is the nominal position when not observing (daytime or bad weather).

The imaging system is built using mass produced commercial components to minimize cost, and does not include any custom electronics or machining (other than cutting and drilling). The durability of the system is a big driver in its design. To keep the system simple and low cost, it does not have a dome: the camera points down when it rains or snows or when there are clouds. The large cylinder around the camera keeps wind down to ensure stable pointing during windy conditions, but also keeps wind from blowing rain particles upward to the camera lens during rainy weather. As the rain falls down into the cylinder, it can drip down the side of the large aluminum plate: there is a gap between the bottom of the cylinder and the top of the aluminum plate, so that the cylinder does not fill up with water. Electronics and power supplies are mounted directly below the aluminum plate so that they are protected from rain and snow. The gentle heat generated by the electronics also hels melt ice and snow on the aluminum plate. The system includes several sensors to determine if the weather is suitable for observing:

- Three webcams acquire images every minute, and are used to automatically confirm nighttime (which is primarily derived from the Sun altitude below the horizon, according to the computer clock). Visual inspection of the webcam images can also identify snow or ice on the mount or camera.
- Temperature probes facing the sky and the ground are used to detect clear sky at night: if the sky is clear, the upward looking temperature probe is colder than the downward looking probe (thermal radiation to the sky). If this temperature difference is larger than a preset limit, then the sky is deemed clear and observing can start.
- A humidity sensor is used to identify wet and humid conditions

In addition to these sensors, the weather information provided by the nearby variable young stellar objects survey (VYSOS) observatory[4] and the the Mauna Loa observatory are downloaded evry minute from the network. Decision to observe is made from all sensor values. The system is designed to minimize the long-term impact of weather :

- No exposed plastic (to avoid UV degradation of plastics)

Figure 2. View of prototype 2 system, pointing South. The Mauna Loa solar observatory is in the background. Openings for the two objectives can be seen on the front of the cameras enclosure. Note that the system does not have a dome, and simply points down during daytime or bad weather. The small shiny box on the right of the camera system is hosting humidity, temperature and cloud sensors.

- The mount has been sealed against water with silicone
- The camera is sealed (cover) except at the front (lens) which points down when weather is bad
- Use of weather-resistant materials when possible: Aluminum instead of steel when possible, Stainless instead of standard steel for bolts/nuts, use of Kapton tape when tape must be exposed.

2.2 Prototype 2 system

In August 2011, prototype 1 was replaced by prototype 2. The improvements between the two prototypes were aimed at improving photometric accuracy, using experience acquired during operation of the first prototype. As shown in figure 2, the new system includes two cameras instead of one, and the new camera has a higher angular resolution (8 arcsec pixels) and its anti-aliasing filter was kept to further reduce pixel sampling errors. The new system is mounted on a sturdy metal frame, and the mount's native drive electronics have been replaced with higher quality stepper drivers: these two improvements greatly reduce tracking errors.

The results presented in this paper are from the first prototype, and it is expected that photometric accuracy will improve with this second prototype.

2.3 Detector characterization: are low cost commercial CMOS detectors suitable ?

The prototype 1 camera system uses a Canon 500D camera body, with a 15Mpix CMOS sensor. Detector characteristics were measured and used to derive the system sensitivity and optimal photon-noise limited exposure times and ISO setting.

Table 2. Measured detector noise and gain for different camera ISO settings. The last column of the table shows the count level for which readout noise is equal to photon noise.

	ISO 100	ISO 200	ISO 400	ISO 800	ISO 1600
Readout Noise [ADU]	10.8959	11.6364	13.9445	19.8761	32.2658
Gain [e-/ADU]	1.36	0.68	0.34	0.17	0.085
Readount Noise [e-]	15.8	7.91	4.74	3.38	2.74
Readout Noise = Photon Noise level [ADU]	161.5	92.08	66.11	67.16	88.49

Results of the measurements are given in table 2 and are in agreement with previous measurements.[5,6] The last column of the table shows the count level for which readout noise is equal to photon noise. Exposures should be sufficiently long to ensure that the background counts are above this level to ensure photon-noise limited performance. The minimum exposure times to ensure photon-noise limited performance are given by combining measured sky background count levels with the previously derived minimum count level to ensure photon-noise limited sensitivity. Under dark conditions, this exposure time ranges from 6.5 sec at ISO 1600 to 190 sec at ISO 100.

2.4 Keeping the cost down

2.4.1 Implementation cost

The combination of a DSLR camera with a high quality commercial lens offers a very attractive cost per etendue compared to more conventional hardware used in astronomy (usually CCD camera + custom optics). The total system cost must also include other hardware such as mount, electronics and computer, which must be taken into consideration during design to keep the cost low. The total cost for the system, including manpower, is estimated at around $14000, with $7713 in hardware and $5600 in manpower (conservatively assuming $100 per hour).

Prototype 2, which is currently starting operation, is somewhat cheaper per etendue, thanks to the fact that two cameras are now mounted on the same mount and share the same computer. The total cost for prototype 2 is about $18000 including manpower, which comes out to $9000 per camera. Fabrication of multiple unit may slightly reduce the cost per unit by reducing manpower requirement per unit and sharing hardware (for example, 4 cameras could be mounted on the same mount). A lower limit of approximately $5000 per camera seems reasonable if many units are fabricated, given that each camera + lens costs almost $3000, and that there are practical limits to how much other hardware can be shared and how little manpower can be devoted to each unit (assembly of components, software installation, troubleshooting scale with number of units). Since each camera offers 0.6 $deg^2 m^2$ of etendue, the cost per etendue is close to $9000 per $deg^2 m^2$.

2.4.2 Operation cost

Keeping the operation cost low requires fully robotic operation of the units and low failure rate, requiring very infrequent maintenance (or no maintenance at all). Failure is defined here as any event which requires physical intervention (computer reboot at site, replacement of a part). With multiple units, some level of failure rate can be tolerated with little increase in operation cost. For example, a failure rate of 10% of the units per year may be acceptable, as a visit to the site every 2 yrs would maintain most of the units functional. Our ongoing work with the prototype system is essential to converge to a system design with high reliability: reliability needs to first be demonstrated on a single (or a small number of) unit(s), and failure points in the design then need to be identified and addressed prior to building and deploying multiple units.

A concern for the operation cost is the large volume of data that needs to be transfered and processed (approximately 2.5GB per night per camera). For a single unit, this data volume is manageable with the network bandwidth available at most observatories, but deployment of a large number of units requires careful planing of data management.

2.5 Lessons learned with prototype 1

2.5.1 System reliability

From late December 2010 to July 2011, our first single camera prototype was in operation at Mauna Loa observatory. The prototype was successfully operated fully robotically from March 2011 to July 2011. In July 2011, the prototype was removed from the site to start upgrade to prototype 2. During the full period (Jan to July 2011), there was one failure requiring visit to the site, when a lightning storm stopped power to the system for longer than the 6 hr capacity of the system's UPS. The system's computer needed to be physically accessed for reboot (no automatic reboot). There was also an incident requiring remote login to the system: during a snow storm, some water found its way in a connector carrying a DC voltage meant to inform the system about the AC power health ahead of the UPS. This lowered the DC voltage below the threshold, and placed the system into safe mode (camera pointing down, to avoid complete stop when the camera is pointing up). This second problem was temporary solved by lowering the voltage threshold in the software, and was later permanently solved by improving the seal around the connector.

2.5.2 System performance

The system performance was satisfactory except for pointing, due in part to the equatorial mount electronics and to the fact that our prototype 1 was mounted on the side wall of a wooden building. While the mount worked reliably, the electronics driving the stepper motors and the communication protocol to the electronics did not easily allow high performance tracking. This problem, combined with the fact that the mounting on a wooden wall did not provide a very stable reference, let to large drifts in pointing (approximately 1" to 5" per mn). This issue is addressed in our second prototype by:

- Mounting the unit on a sturdy metal frame, directly bolted to a ground concrete pad
- Replacing the native mount electronics with stepper controller+driver circuits offering more fine control of pointing and tracking (allowing for example small updates in tracking speed without introducing unwanted jumps/interruptions in the tracking)
- Implementing closed loop guiding: the images acquired are continuously used to refine pointing and tracking

3. CALIBRATING INSTRUMENTAL ERRORS WITH THE REMOVE, REPLACE AND COMPARE (RRC) ALGORITHM

3.1 Description photometric data reduction approach and challenges

Our photometric measurement is differential: other stars in the field are used to construct a reference against which the target star is compared. Choosing the optimal of PSF(s) used for comparison with the target star is essential to compensate for error terms correlated with other sources (variable extinction due to clouds and airmass, color effects, detector non-linearity). The choice of the comparison PSFs is therefore critical to achieving photometric precision, and is complicated by the detector's undersampling of the PSF, discussed in the next paragraph.

The main challenge to precision photometry with a low-cost DSLR-based system is to overcome errors due to PSF sampling, which are particularly serious in our system, as the pixel size is comparable to the PSF size, and the pixels are colored (25% of pixels are red-sensitive, 50% are green-sensitive and 25% are blue-sensitive). This issue could be mitigated by defocusing the image, thus spreading light of each star on many pixels. For example, defocusing star images to a 35 pixel diameter disk, Littlefield[2] reports achieving 1% photometric accuracy in each of the 3 detector color channels over 90 sec exposures with a 203 mm telescope, and measuring transit depth to 0.1% (1 millimagnitude) for a 1hr duration transit. While this scheme is appropriate for photometry of a small number of bright stars, it is not suitable for a transit survey aimed at monitoring a large number of stars, as the combined loss of angular resolution (crowding limit) and faint-end sensitivity (mixing starlight with background) would have a large impact on the survey performance.

In addition to the PSF sampling issue, a large number of variables can affect the measured apparent flux from stars (for example airmass, color extinction effects, PSF variations). Comparison PSF(s) used for differential photometry must be chosen to include these effects, either by choosing stars which are subjected to the same errors, or by understanding, modeling and compensating for these effects.

3.2 Modeling vs. Statistical "Lucky PSF" approach

The challenges listed in the previous section could be addressed by PSF modeling and analysis of sources of photometric error, as is often done for precision photometry with imaging arrays. This analysis would constrain both the choice of the ideal comparison PSF(s) to perform differential photometry, and how to compensate for residual errors. For example, the effect of PSF color on the photometric signal could be estimated (either empirically from the data or by modeling), the colors of PSFs in the field estimated, and the best comparison PSFs could be then be chosen according to this analysis. Other effects would be treated in a similar way, and the final choice of the comparison PSF would rely on combining the results of several such analyses. The PSF undersampling issue would be mitigated by PSF shape modeling and analysis of how PSF location at the sub-pixel scale affects the photometric measurement.

A simpler and more powerful approach is to use the large number of PSFs in the field to automatically select the best comparison PSFs with no modeling of errors. The target PSF images acquired before and after (but not during) the transit to be tested are compared with all other PSF images in the field, and the selection of the best comparison PSF(s) is based upon choosing PSF(s) that best matches the target PSF images. The selection is not affected by the transit, as the image(s) of the target during the transit are not used for the selection. This technique uses the powerful statistical argument that **in a sequence of wide field images, there must be at least one "Lucky" PSF which experiences the same errors as the target** (a PSF which has the same brightness, same color, falls on the same fractional pixel position, etc...). Rather that trying to identify such PSF(s) by measuring relevant parameters (color, PSF position, etc..) and relying on model(s) to understand how these parameters affect the photometric measurement, our algorithm empirically perform the identification by comparing images of the target star with other stars in the field, and does not require knowledge of what are the physical processes producing errors in the photometry. This selection must be done at the image level, and should not be done at the lightcurve level: since multiple sources of errors contribute to an aperture photometry measurement, several independent effects might cancel each other in the aperture photometry data (for example PSF shape, color, pointing) during the set of images used for identification of the reference PSF(s), while they would not cancel during the transit.

3.3 Algorithm description

3.3.1 Testing transits instead of working from lightcurves

The algorithm we propose to use does not rely on building a light curve and then identifying transits in the light curve (as is usually done). Instead, we seek to test a transit hypothesis for a given choice of transit parameters (transit duration and phase): did a transit occur at phase phi, period P, and of durationd d ? The metric computed is the estimated transit depth for this particular choice of transit parameters. We scan the transit parameters (phase, period and duration) to measure the estimated transit depth across the 3-D space defined by the parameters. If no transit occurs, the resulting 3-D map contains noise, with approximately as many positive values as negative values.

This approach offers fundamental advantages over the conventional approach of working from lightcurves. The optimal data analysis parameters should ideally be a function of the transit parameters, but a lightcurve based approach fixes these parameters across the time span during which the lightcurve is computed. Detrending techniques working from lightcurves[7,8] are aimed at mitigating this limitation, but do not offer full flexibility. For example, the choice of the best PSFs for comparison should ideally maximize correlation between the target PSF and reference PSF(s) excluding the time during which the transit occurs. As the transit phase or duration changes, the criteria for the choice of the best reference PSF(s) will therefore also change, and the algorithm should ideally be able to pick different comparison PSF(s) as these parameters change.

3.3.2 Step by step description of the algorithm

- STEP 1 - **Choose a set of transit parameters (phase, period and duration)**. The purpose of the steps below is to test if the transit matching these parameters occured. The metric used is the transit depth, computed at the end of the process.

- STEP 2 - **Separate the images of the sequence in two groups: group A consists of all images during the transit, group B consists of all the images outside the transit**

- STEP 3 - **Use all images in group B (outside transit) to identify PSF(s) in the field which best match the target PSF**. The identification is done directly from the images (no photometry, no lightcurve), using the sum square difference between target images and PSFs as a minimization criteria. For example, the following criteria may be used:

$$V(ii,jj) = \sum_{i=0}^{n-1} \left[\sum_{ii1^2+jj1^2<radius^2} (B_i(ii0+ii1, jj0+jj1) - B_i(ii+ii1, jj+jj1))^2 \right] \tag{1}$$

  where i is the image index within set B, n is the number of images in set B, $B_i(ii,jj)$ is the pixel value for pixel (ii,jj) in image i within the group B, $(ii0,jj0)$ is the location of the target star, and radius denotes the size over which the pixels are compared. The value $V(ii,jj)$ then represents how well, within the group B of images, the pixel values around pixel (ii,jj) match the pixel values around pixel $(ii0,jj0)$ - where the target star is located. We note that $V(ii0.jj0) = 0$, and that a small value for $V(ii,jj)$ indicates that a star which behaves similarly to the target star is located on pixel (ii,jj). The equation may be refined to include flux scaling (allow for comparison of stars of difference brightnesses), and weighting factors that take into account noise properties (readout noise, photon noise) or other known limitations.

- STEP 4 - **Construct a reference PSF image sequence during the transit**. The value(s) of (ii,jj) for which $V(ii,jj)$ is smallest is(are) used to build this sequence. For example, if the single smallest value of $V(ii,jj)$ (other than the trivial $ii = ii0$, $jj = jj0$ solution) is obtained for $(ii,jj) = (ii_{min}, jj_{min})$, then :

$$RefPSF_j(ii,jj) = \alpha A_j(ii+ii_{min}, jj+jj_{min}) \tag{2}$$

  where α is adjusted to best match the photometry of the target and reference PSF outside transit (group B), and j is the image index within group B (during transit).

- STEP 5 - **Derive the estimated transit depth a by comparison of the target PSF and reference PSF during transit**. An estimate of the transit depth a may be obtained by:

$$(1+a) = \left(\sum_{j=0}^{m-1} \sum_{ii1^2+jj1^2<radius^2} A_j(ii0+ii1, jj0+jj1) \right) / \left(\sum_{j=0}^{m-1} \sum_{ii1^2+jj1^2<radius^2} RefPSF_j(ii1, jj1) \right) \tag{3}$$

  Where m is the number of images in group A. This equation may be improved by optimal weighting of pixel values.

4. PRELIMINARY ON-SKY RESULT

4.1 Test dataset

The star HD 54743 ($m_V = 9.39$) was observed on 2011-04-15 (UT) with the robotic imaging system described in section 2. Figure 3 shows the part of a single raw image around HD 54743. Thirty consecutive 65-sec exposures were acquired at ISO100, as shown in figure 4. The images were acquired during bright time, with a relatively strong background (level = 2500 ADU, 2600 ADU and 1900 ADU per pixel per exposure in R, G and B respectively).

This dataset is especially challenging for photometry, as the PSF is strongly undersampled (in part due to the fact that the camera's anti-aliasing filter has been removed), the detector is a color CMOS array, and the tracking is relatively poor, with a drift of approximately 5" per minute (0.5 pixel between consecutive frames).

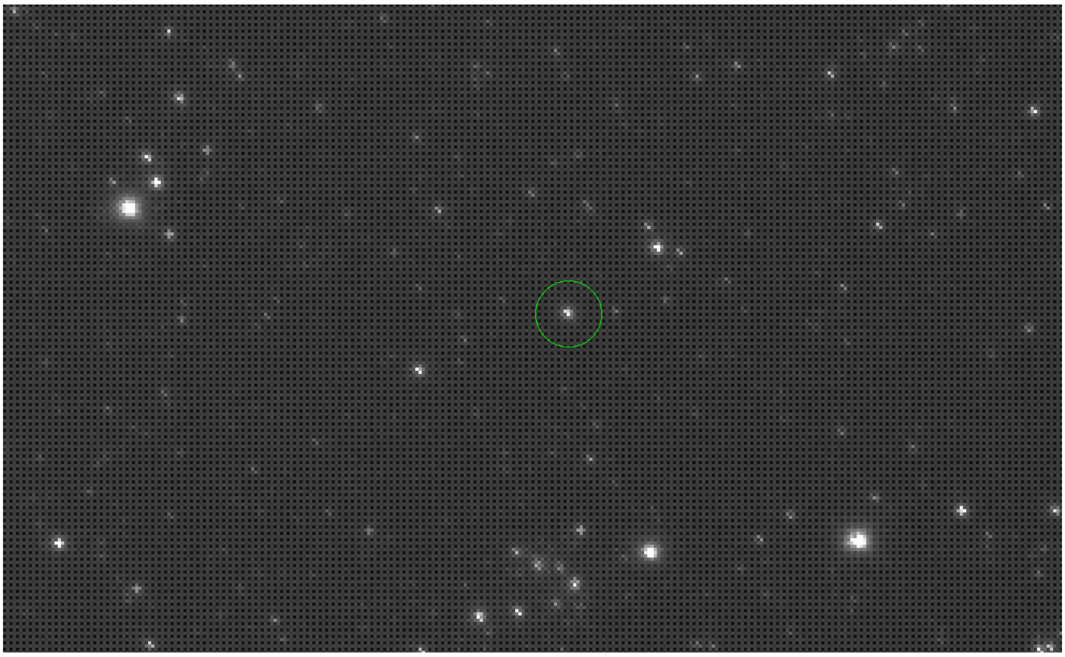

Figure 3. Part of a single 65-sec image of the HD 54743 field. The green circle shows the location of HD 54743. Pixels are 10 arcsec wide.

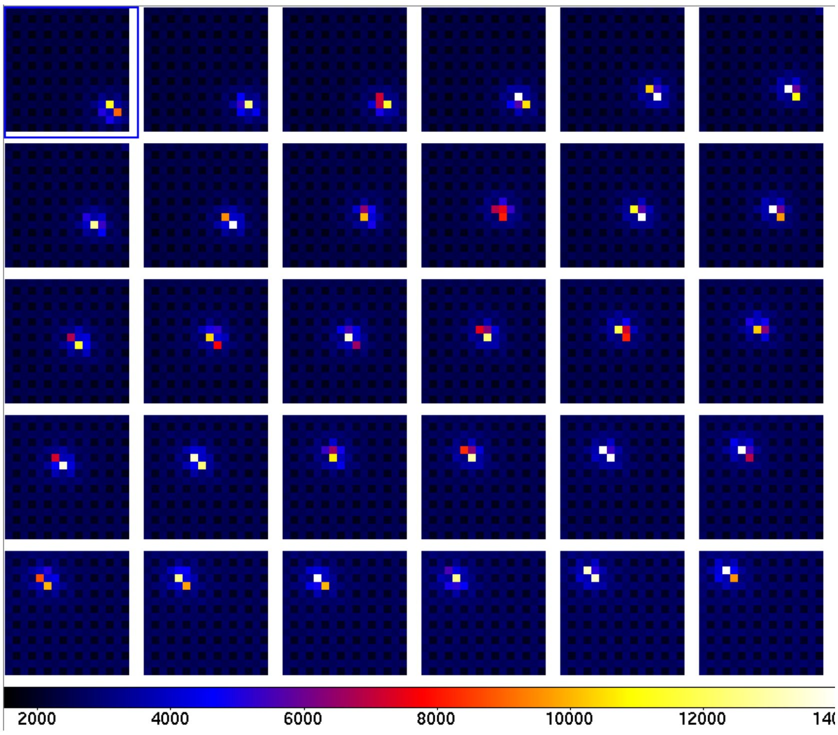

Figure 4. Sequence of 30 consecutive RAW images, showing the 16 pixel x 16 pixel detector area around star HD54743. The Bayer color array is visible in the raw data: the dark background pixels (1 pixel out of 4) are the B channel, and the brighest background pixels are the G channel (1 pixel out of two); the remaining pixels are the R channel.

4.2 Performance: Conventional Aperture photometry vs. RRC algorithm

Aperture photometry results for the dataset are shown on the first line of table 3 (showing standard deviation). The measured standard deviation in each of the 3 color channels is significantly larger (2x to 6x depending on the color) than the combined effect of known fundamental noises (photon noise, readout noise, scintillation and flat field error). This is due to the undersampling of the PSF by the color detector array. Figure 4 shows that the PSF is about one pixel wide, and that if it is centered on a pixel, the corresponding color will be artificially enhanced in aperture photometry. Since the standard deviation is dominated by this sampling effect, the values can be interpreted as a measure of this effect alone. Interestingly, the R channel standard deviation is smaller than either the G or B channels. Close inspection of the data shows that this is due to the fact that the PSF is wider in the R band than in other colors, and sampling errors are therefore smaller in this band. The sampling error is largest in the G channel, even though this channel has twice as many pixels as either R or B channels: the PSF is much sharper in the G color than other colors.

Table 3. Photometric Performance: conventional aperture photometry and RRC algorithm compared

	R channel	G channel	B channel	notes
Average count (ADU)	5918.4	25990.6	6658.04	aperture photometry
Conventional Aperture photometry	**4.72%**	**13.56%**	**11.24%**	
RRC algorithm	**2.48%**	**2.04%**	**3.51%**	
Photon noise limit	2.79%	1.00%	2.24%	
Total error expected	2.88%	1.14%	2.42%	

The same dataset was also processed with the RRC algorithm. For each image i in the dataset, the assumption to be tested was: "Did a transit occur during, and only during, frame i". Group A (during transit) therefore consists of frame i, and group B (outside transit) consists of all other frames. For each i, the transit depth was estimated. Figure 5 shows a key step in the algorithm, with i=15. The target PSF during the hypothetical transit is shown on the left: this is the data that is removed. All other data (other frames + frame number 15 excluding the target PSF) is then used to build an estimate of what the target PSF should be on frame 15. This template is shown on the right part of the figure, and replaces the missing data. Comparison of the removed data and replacement leads to a photometric estimate of the transit depth, if the transit occured during frame number 15. In this particular example, the template is built from an optimal linear combination of the 80 PSFs in the field which best match the target PSF.

Photometric estimates for each of the 3 color channels are shown for both the conventional aperture photometry and the lucky PSF RRC algorithms on figure 6. We note that the result obtained by the lucky PSF RRC algorithm is not exactly a light curve; instead, it is the estimated transit depth for a transit duration of exactly one frame.

The achieved photometric precision in each color channel is given in table 3: it is at the photon noise limit level for the R channel, 60% above photon noise limit for the B channel and at twice the photon noise limit in the G channel. The expected photometric precision, including photon noise, readout noise, flat field errors but assuming no PSF sampling error term or atmospheric extinction, is given for comparison, and shows that our algorithm reduces sampling errors at the level of, or below, other dominant sources or errors.

5. CONCLUSION

The success of an exoplanet transit survey program relies on the ability to monitor a large number of targets with high photometric precision. While space-based missions have the advantage of providing a highly stable environment, a large number of units can be deployed inexpensively on the ground to average down errors and weather. The keys to achieving high photometric precision in a ground-based transit survey are therefore to (1) deploy a large number of reliable robotic units at a competitive cost and (2) reduce for each unit the noise level, if possible approaching or reaching the photon noise limit. Assuming that noise can be reduced to the fundamental

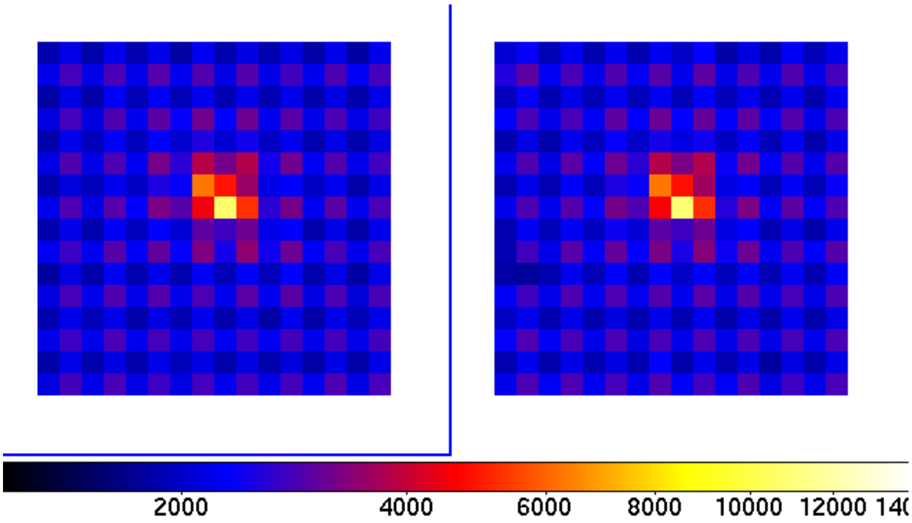

Figure 5. Left: Target PSF number 15 (HD 54743 image extracted from frame number 15 - this PSF can also be seen in Figure 4, noting that index starts at 0 at the top left of the figure). Right: Template reconstructed from other PSFs in the field. The template is compared to target PSF number 15 to derive photometry. The template is obtained from a linear combination of PSFs other than the target, and the linear coefficients used to build it were computed after removal of target PSF 15 from the dataset. Derivation of the template shown on the right is therefore fully independant of the target PSF number 15 shown on the left. The match between the two PSFs is good at the few percent level.

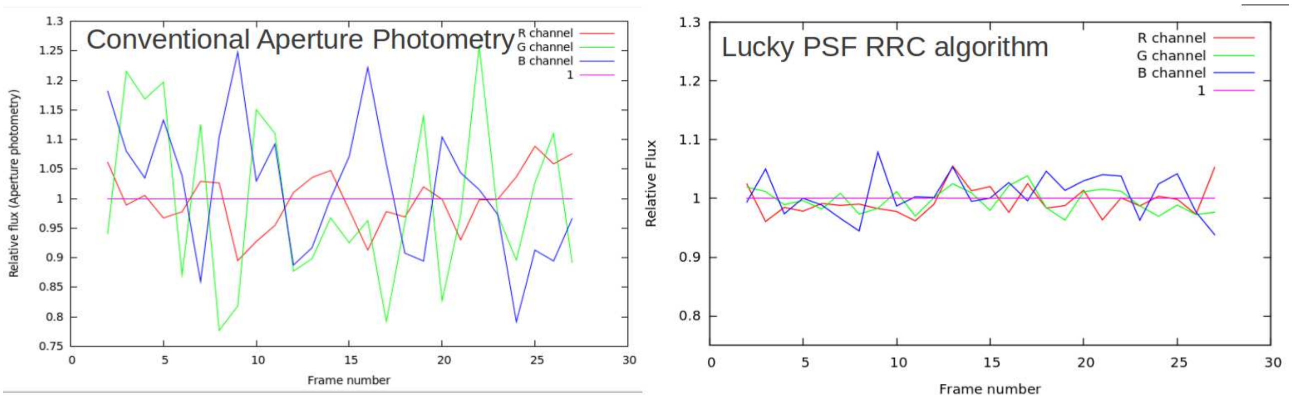

Figure 6. Left: Photometric light curve derived with aperture photometry, with each frame corresponding to a 65 sec long exposure. Right: Light curve obtained with the same data using the lucky PSF replace remove and compare algorithm.

limit imposed by photon noise, the performance of an exoplanet transit survey is then entirely driven by total etendue (product of field of view by collecting area multiplied by the number of units). This edendue can then be allocated to a deep survey of a small fraction of the sky or a shallower survery of a large fraction of the sky, depending on the scientific goals.

We have shown in this paper that commercially available digital single lens reflex (DSLR) cameras using low noise CMOS arrays offer a highly reliable and cost-effective approach to obtain large etendue, at a cost below $10k per square meter square deg of etendue. Our results demonstrate that (1) these low cost cameras can be scientifically valuable thanks to attractive detector performance (low noise), (2) a robotic DSLR-based system can be build and operated reliably at a small cost and with a small failure rate, and (3) a statistical approach to photometry analysis of wide field images can almost eliminate sampling and color effects in DSLR cameras, turning them into high precision photometers. Together, these three points demonstrate the value of an approach where a high number of DSLR-based units, potentially similar to the prototype described in this paper, would perform a photometric survey of a large fraction of the sky.

ACKNOWLEDGMENTS

This project was made possible thanks to Bo Reipurth and Josh Walawender of the Variable Young Stellar Object Survey (VYSOS) project, and the Mauna Loa observatory. Paul Stewart (University of Sydney) provided valuable help to install the system. Josh Walawender allowed the system to use VYSOS's weather monitoring and provided assistance in setting up the hardware at the site.

REFERENCES

[1] Fiacconi, D. and Tinelli, L., "Light curve analysis of XX Cygni from data taken using DSLR," *Open European Journal on Variable Stars* **114**, 1–+ (Oct. 2009).

[2] Littlefield, C., "Observing Exoplanet Transits with Digital SLR Cameras," *Journal of the American Association of Variable Star Observers (JAAVSO)* **38**, 212–+ (Dec. 2010).

[3] Hoot, J. E., "Photometry With DSLR Cameras," *Society for Astronomical Sciences Annual Symposium* **26**, 67–+ (May 2007).

[4] Walawender, J., Reipurth, B., and Paegert, M., "Computer Infrastructure for the Variable Young Stellar Objects Survey," *Proceedings, Telescopes from Afar, March 2011* (2011).

[5] Buil, C., "Spectroscopy, CCD and Astronomy," *http://www.astrosurf.org/buil/* (2011).

[6] Clark, R. N., "Digital Camera Sensor Performance Summary," *http://www.clarkvision.com/imagedetail/digital.sensor.pe* (2011).

[7] Kovács, G., Bakos, G., and Noyes, R. W., "A trend filtering algorithm for wide-field variability surveys," *MNRAS* **356**, 557–567 (Jan. 2005).

[8] Tamuz, O., Mazeh, T., and Zucker, S., "Correcting systematic effects in a large set of photometric light curves," *MNRAS* **356**, 1466–1470 (Feb. 2005).